Biomedicine & Pharmacotherapy 200 (2026) 119485

Contents lists available at ScienceDirect

Biomedicine & Pharmacotherapy

journal homepage: www.elsevier.com/locate/biopha

Modeling osteosarcoma invasion with fibroblast and tumor spheroids in functionalized hydrogels beads

M. Rossi [a,b,*,1], L. Anconelli [a,b,1], M.M. Rydzyk [a], A. Crea [a], F. Rossi [a], E. Coschina [a], G. Ravegnini [a,c], G. Ulian [d,e], G. Valdrè [d,e], M. Montesi [f], D. Gardini [f], C. Cappadone [a], P. Blasi [a,b], S. Iotti [a,g,2], E. Malucelli [a,2]

[a] Department of Pharmacy and Biotechnology, Alma Mater Studiorum University of Bologna, Bologna, Italy
[b] Center for Applied Biomedical Research (CRBA), Alma Mater Studiorum University of Bologna, Bologna 40126, Italy
[c] Clinical Pharmacology Unit, IRCCS Azienda Ospedaliera-Università di Bologna, Bologna, Italy
[d] Biological, Geological and Environmental Sciences, Alma Mater Studiorum University of Bologna, Bologna, Italy
[e] Interdisciplinary Centre of Biomineralogy, Crystallography and Biomaterials, Alma Mater Studiorum University of Bologna, Bologna, Italy
[f] Institute of Science, Technology and Sustainability for Ceramics, National Research Council of Italy, Faenza, Italy
[g] INBB National Institute of Biostructures and Biosystems, Rome, Italy

ARTICLE INFO

Keywords:
3D Cell Culture
Hydrogel beads
Tumor microenvironment
Licochalcone A
MG63
143B

ABSTRACT

Osteosarcoma (OS) is a highly aggressive bone tumor with a strong propensity for metastasis. To develop a physiologically relevant *in vitro* platform for tumor invasion studies and drug testing, we engineered a three-dimensional OS model that mimics the tumor microenvironment using hydrogel-based multicellular spheroid beads. Tumor spheroids (~125 μm) were generated and co-cultured with WS1 fibroblasts in VitroGel® RGD, a hydrogel matrix that promotes cell adhesion via integrin binding. The hydrogel beads, approximately 2–3 mm in size, supported robust growth of both MG63 and highly metastatic 143B cells. Notably, 143B spheroids exhibited pronounced invasion into the matrix, recapitulating their aggressive phenotype. To evaluate therapeutic potential, the antitumoral compound Licochalcone A (Lic-A) was applied to beads at varying concentrations. Lic-A induced a dose-dependent reduction in metabolic activity and membrane integrity, with minimal cytotoxic effects on stromal fibroblasts. Gene and protein expression analyses revealed that Lic-A significantly downregulated Ki67 and MMP-9, while increasing BMP2 and VEGF-C expression. Interestingly, vimentin mRNA was upregulated, yet its filamentous structure was disrupted, indicating stress- or apoptosis-related cytoskeletal remodeling. Live-cell imaging and SEM confirmed extensive 143B cell invasion, along with cytoskeletal changes and ECM degradation. Altogether, this study establishes a scalable 3D OS model that captures key features of the tumor-stroma interface and supports dynamic invasion processes. The model demonstrates the multifaceted anticancer effects of Lic-A and provides a valuable platform for studying OS biology and testing anti-metastatic therapies in a biomimetic setting.

1. Introduction

Osteosarcoma (OS) is the most common primary malignant bone tumor in children and adolescents, characterized by aggressive local growth and a high propensity for metastasis, particularly in the lungs. Despite advancements in surgical techniques and chemotherapeutic regimens, the prognosis for patients with metastatic or recurrent OS remains poor, highlighting the urgent need for more effective therapeutic strategies [1,2].

Traditional two-dimensional (2D) cell culture systems, while widely utilized in cancer research, fail to recapitulate the complexity of the tumor microenvironment observed *in vivo*. Three-dimensional (3D) culture models offer a more physiologically relevant platform by mimicking key aspects of tumor architecture, including 3D cell-cell and cell-extracellular matrix (ECM) interactions, nutrient and oxygen gradients, and hypoxic conditions. These models have proven invaluable in

* Correspondence to: Department of Pharmacy and Biotechnology, Alma Mater Studiorum University of Bologna, via San Donato 19/2, Bologna 40127, Italy.
E-mail address: martina.rossi12@unibo.it (M. Rossi).
[1] These authors contribute equally
[2] These authors contribute equally

https://doi.org/10.1016/j.biopha.2026.119485

Available online 14 May 2026

exploring tumor biology, drug resistance, and therapeutic responses [3,4]. The ECM is a critical component of the tumor microenvironment, providing structural support and biochemical signals that regulate cell behavior. The ECM influences tumor progression, metastatic potential, and treatment response, making it central for therapeutic development [5].

Furthermore, the inclusion of multiple cell types into 3D culture models, such as fibroblasts, endothelial cells, and immune cells, enables more accurate recapitulation of the *in vivo* tumor niche [6]. These heterotypic interactions are essential for studying the metastatic process, including epithelial-to-mesenchymal transition (EMT), invasion, intravasation, immune evasion, and colonization at distant sites like the lungs, providing useful information for identifying new therapeutic targets [7].

As far as OS is concerned, 3D culture systems have become particularly valuable due to their complex microenvironment, which includes not only the tumor cells themselves but also interactions with bone matrix components and various stromal cells. Unlike cell monolayers, 3D models better simulate the native bone architecture and mechanical stiffness. These conditions influence critical aspects of tumor biology, such as proliferation, invasion, and resistance to chemotherapeutic agents [7,8]. For example, 3D spheroids and scaffold-based models have demonstrated that OS cells exhibit reduced sensitivity to drugs compared to cell monolayers, better mirroring the clinical scenario of chemoresistance [9,10]. Furthermore, 3D co-culture systems incorporating stromal cells, osteoblasts, or immune cells provide a more comprehensive platform for studying tumor-stroma interactions and metastatic mechanisms [11]. Such models are increasingly employed in preclinical drug screening and mechanistic studies, offering a promising bridge between traditional cell culture and *in vivo* experimentation.

In this scenario, to address the need for physiologically relevant 3D models of OS, we developed a model based on VitroGel® RGD encapsulation, co-culturing tumor spheroids and fibroblasts to mimic the tumor microenvironment and assess the invasiveness. To evaluate the developed model, Licochalcone A (Lic-A) was used as a test compound. Lic-A, a naturally occurring chalcone derived from *Glycyrrhiza* species, has been reported to exert anti-tumor effects in multiple cancer models by suppressing proliferation, inducing apoptosis, and inhibiting metastasis, mechanisms that have been associated with the modulation of signaling pathways such as PI3K/Akt, MAPK, and NF-κB. However, its activity within complex three-dimensional tumor microenvironments remains less explored [12].

2. Materials and methods

2.1. Cell lines and culture conditions

The human OS cell lines MG63 and 143B, and the human dermal fibroblast WS1 were acquired from the American Type Culture Collection (ATCC, Manassas, VA, USA). Human bone marrow–derived mesenchymal stromal cells (BM-MSCs) were obtained from Lonza (Basel, Switzerland) and cultured according to the manufacturer's instructions. Cells were cultured in Dulbecco's modified Eagle medium (DMEM) supplemented with D-glucose (4.5 g/L), 10% fetal bovine serum (v/v), L- glutamine (2 mM), penicillin (100 U/ml) and 1 mg/ml of streptomycin (Microtech, Pozzuoli, Italy). Cells were routinely grown in 5% CO_2/humidified air at 37 °C. To monitor cells during experiments, one of the three cell lines, depending on the experiment, was stained with Vybrant DiO green fluorescence dye (Invitrogen, Thermo Fisher Scientific, Waltham, MA, USA) following manufacturer instructions.

2.2. 3D cell culture generation

To generate spheroids of uniform shape and size, Corning® Elplasia™ 24-well microplates (Corning, NY, USA) were used. Each well consists of 554 identical microcavities, enabling the formation of multiple consistent spheroids. Specifically, 125000 cells per well, corresponding to approximately 225 cells per microcavity, were seeded for both MG63 and 143B cell lines. After seeding, the plate was centrifuged at 100 × *g* for 3 min to promote cell aggregation at the bottom of each microwell. The plate was then incubated at 37°C in 5% CO_2. After 3 days, the resulting spheroids were collected and combined with 5 * 10^5 single WS1 fibroblast cells or BM-MSCs. The mixture was centrifuged and resuspended in 100 μL of complete culture medium. Subsequently, 50 μL of this cell suspension was mixed with 200 μL of VitroGel® RGD hydrogel high concentration (The Well Bioscience Inc., Monmouth Junction, NJ, USA), previously diluted 1:1 (v/v) with VitroGel® Dilution Solution Type I. Hydrogel beads were formed by dispensing the mixture drop by drop using an insulin syringe into U-bottom 96-well plates containing 100 μL of complete medium per well. After 15 min of incubation under sterile conditions, bead formation was confirmed microscopically, and images were acquired at various time points. While spheroids are compact 3D aggregates of tumor cells grown in suspension or within microcavities, hydrogel beads refer to these spheroids embedded within a hydrogel matrix, providing a microenvironment that mimics *vivo* tissue structure.

2.3. Metabolic activity

The reduction capacity was measured by the resazurin assay. Samples were incubated with a 100 μM solution of resazurin for 5 h at 37°C and the fluorescence was measured at 560 nm excitation and 590 nm emission in a microplate reader (Ensight Multimode Plate Reader, Perkin Elmer, Waltham, MA, USA).

2.4. Treatment with licochalcone A

The 3D models were treated with Lic-A (Sigma Aldrich Co., St. Louis, MO, USA) at the IC_{50} concentration, which, according to our previous studies, was 120 μM for MG63 and 80 μM for 143B [13]. 143B was also treated with increasing concentrations of Lic-A, specifically 80, 40 and 20 μM. After 48 h of incubation, viability staining and the Resazurin test were performed.

2.5. Viability assay

To determine hydrogel bead viability, cells were stained with a 2 μg/ml solution of Hoechst 33342 and a 5 μg/ml solution of propidium iodide (PI). After 45 min of incubation at 37°C, images were acquired by confocal microscopy. Acquisitions were performed using an λexc 405 nm and λem 450/35 nm for Hoechst, an λexc 488 and λem 515/30 nm for DiO (green stained fibroblasts) and an λexc 543 and λem 650 nm for PI respectively. Images were acquired by a confocal microscope (Nikon, Eclipse C1, Nikon instrument S.p.A, FI, Italy).

2.6. 143B model characterization

To further characterize 143B cell invasion, hydrogel beads were also monitored by the live-cells analysis system IncuCyte® (Essen BioScience Ltd, Hertfordshire, UK). Phase and green fluorescence images were then acquired every 4 h for 36 h through the IncuCyte® live imaging systems. Spheroid dimensions and invasions were determined through Incucyte® Software (v2024A).

Hydrogel beads were fixed in 10% formalin, washed in PBS and then F-actin filaments were fluorescence-labelled with phalloidin (Sigma Aldrich Co., St. Louis, MO, USA, P5282–1MG). Phalloidin was used at 1 μg/ml together with Hoechst 33342 at a concentration of 2 μg/ml and incubated for three hours at room temperature (RT). Images were then taken through a confocal microscope (Nikon, Eclipse C1, Nikon instrument S.p.A, FI, Italy).

2.7. Dynamic mechanical analysis (DMA)

Dynamic mechanical analysis (DMA) was performed on all the samples (with and without the cells) at different incubation times (1, 5 and 7 days) to determine Young's modulus with a dynamic mechanical analyzer (DMA Q800, TA Instruments). The Young's modulus was evaluated from the slopes of the stress-strain curve obtained in compressive mode at 37 °C with the samples submerged in PBS 1X. The measurements were repeated three times for each sample (n = 3). A linear regression of the points in the initial linear regions was performed to obtain the slopes. The first points measured are often affected by instrumental errors and were excluded from the analysis.

2.8. Environmental scanning electron microscopy

After 4 and 10 days of culture, hydrogel beads were rinsed three times with PBS and fixed in 10% formalin for 3 h at RT. The samples were then frozen at −80 °C overnight, followed by freeze-drying at 0.01 atm and −45 °C using a freeze dryer (ALPHA 1–2, Christ, Milan, Italy) for 24 h. Finally, images were acquired using an Environmental Scanning Electron Microscope, ESEM (QuattroS, Thermo Fisher Scientific, Waltham, MA, USA) equipped with a Field Emission Gun (FEG-ESEM). After a careful calibration [14,15], a low-vacuum condition of 100 Pa and an acceleration voltage of 10 kV were employed.

2.9. Lactate dehydrogenase assay

Cytotoxicity was estimated based on the activity of the cytosolic enzyme lactate dehydrogenase (LDH) in the culture medium and compared to the activity of cultured cells. The LDH activity was determined in the medium collected after 48 h of treatment. In brief, hydrogel beads media were collected and centrifuged at 4000 x g to remove cells and debris and transferred in a 96 well plate. After this, 132 μL Potassium Phosphate 0.1 M (pH=7.5), 5 μL Sodium Pyruvate 23 mM, 10.5 μL of media and 2.5 μL NADH 14 mM in TRIS 0.1 M (pH=7.0) were added in each well, following this order. The absorbance of the samples was measured at 340 nm every 30 s in a plate reader (Ensight Multimode Plate Reader, Perkin Elmer, Waltham, MA, USA).

2.10. Gene expression

To isolate total RNA, seven hydrogel beads were first incubated with the TRIzol Reagent (Thermo Fisher Scientific, Waltham, MA, USA) at −80°C overnight and the day after, manufacturer's protocol was followed to complete the isolation; cDNA was retrotranscribed by the High-capacity RNA-to-cDNA™ Kit (Applied Biosystems™) according to the manufacturer's instructions. Expression levels of target genes were quantified by real-time (RT)-PCR using PowerUp™ SYBR™ Green Master Mix (Applied Biosystems, Thermo Fisher Scientific, Waltham, MA, USA) in a QuantStudio 7 Real-Time PCR System (Applied Biosystems, Thermo Fisher Scientific, Waltham, MA, USA). Relative expression was estimated by the 2^-ΔΔCt method, using GAPDH as housekeeping control. RT-PCR experiments were run in triplicate. The primer sequences of target genes are listed in Table 1.

Table 1
Real time PCR Primer sequences.

Genes	Forward primers	Reverse primers
Ki67	AGGCAAAGAAGACCTGCTACT	AGTTTGCGTGGCCTGTACTA
MMP2	CATGAAGCCCTGTTCACCAT	TCAGTGGTGCAGCTGTCATA
MMP9	CCAACTACGACCGGGACAAG	ATCACCGTCGAGTCAGCTC
VIM	CCCTCACCTGTGAAGTGGAT	TAGCAGCTTCAACGGCAAAG
COL1A1	GATCTCCTGGTGAAGCTGGT	GGCTTCCAGTCAGACCCTT
BMP2	CCAGCCGAGCCAACACTG	TCCCACTCGTTTCTGGTAGT
VEGFA	GCCTTGCTGCTCTACCTCCA	TCCACCAGGGTCTCGATTGG
VEGFC	GTCCGGACTCGACCTCTCG	CAGACCGTAACTGCTCCTCCA
GAPDH	GAAGGTGAAGGTCGGAGTCAAC	TGGAAGATGGTGATGGGATTTC

2.11. Immunofluorescence staining

The 143B hydrogel beads were fixed in 10% formalin, washed in PBS and then fluorescence labelling of metalloproteinases (MMP-9 and MMP-2), BMP-2, Vimentin (VIM) and COL1A1 were performed at the concentrations shown in Table 2. To carry out the staining, cell membranes were permeabilized with PBS triton-100 0.2% (v/v) (Sigma Aldrich Co., St. Louis, MO, USA). Subsequently, three washes in PBS were performed and the binding sites were saturated with PBS-BSA 1% (w/v) (Sigma Aldrich Co., St. Louis, MO, USA). Subsequently, the primary antibody was added and incubated overnight at 4°C. After three washes in PBS, the secondary antibodies shown in Table 2 were added together with Hoechst 33342 dye at a concentration of 2 μg/ml and incubated for three hours at RT. Finally, three washes in PBS were performed and observation under a confocal microscope (Nikon, Eclipse C1, Nikon instrument S.p.A, FI, Italy) was continued.

2.12. Statistical analysis

Data are reported as means ± SD of at least three independent experiments, and all treatments were analyzed against control. A paired *t*-test or a one and two-way ANOVA corrected for multiple comparisons (Dunnett test) was performed with GraphPad Prism software (GraphPad Software, version 10.0.2, San Diego, CA, USA) (www.graphpad.com). Significance was graphically reported as follows: * $p < 0.05$, ** $p < 0.01$, and *** $p < 0.001$.

3. Results and discussion

3.1. Hydrogel beads production

With the goal of establishing an *in vitro* OS model mimicking the tumor microenvironment, hydrogel beads were generated. After testing different matrices, Vitrogel® RGD was chosen since RGD (Arg-Gly-Asp) domain promotes cell adhesion and growth through binding to integrin receptors especially for the fibroblast counterpart [16]. The project's overall workflow is summarized in Fig. 1. Briefly, spheroids from MG63 and 143B were produced, combined with fibroblasts and embedded in hydrogel. Finally, after 5/7 days, hydrogel beads were treated with Lic-A.

More in detail, tumor spheroids of uniform size and morphology were produced. Additionally, small-sized spheroids were required to ensure the passage through an insulin syringe needle during dropping. The spheroid dimensions were measured and monitored over time, resulting in spheroids with an average diameter of approximately 125 μm. Images and related data are presented in Fig. 1**S**. After 48 h, the

Table 2
Antibodies.

Antibody	Seller	Code	Host	Working concentrations
Anti- MMP-2	STJ laboratories	STJ28003–100	Rabbit	1:200
Anti-MMP-9	STJ laboratories	STJ98248–100	Mouse	1:500
Anti-BMP-2	STJ laboratories	STJ500263–100	Rabbit	1:200
Anti-Vimentin	Cell signaling	#5741	Rabbit	1:100
Anti- COL1A1	Elabscience	E-AB-40334	Rabbit	1:100
Cy3 anti-mouse	Jackson	115–165–166	Goat	1:400
Anti-rabbit AlexaFluor 546	Life Technologies	A11035	Goat	1:250

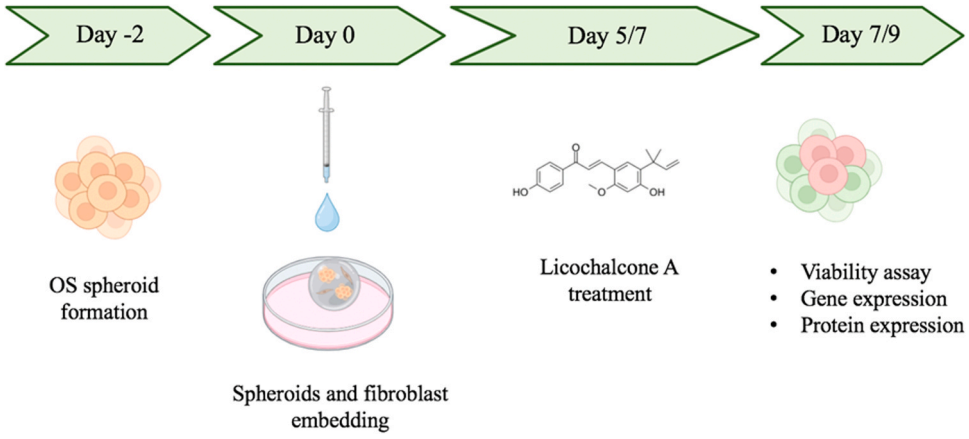

Fig. 1. Project workflow.

spheroids were combined with WS1 human dermal fibroblasts and hydrogel to generate hydrogel beads (Fig. 2**A**). Fig. 2**B** shows a macroscopic image of a representative hydrogel bead with a diameter of 2–3 mm. Microscopic images showing spheroid growth at various time points are provided in Fig. 2**C**, while the corresponding metabolic activity is displayed in Fig. 2**D**.

The results indicate substantial cell growth for both cell lines. Notably, for 143B, cell invasion was observed, with the cells progressively occupying the entire surrounding matrix (Fig. 2**C**). This behavior is consistent with previous reports, as 143B is recognized as one of the most metastatic OS cell lines [17]. The ability of 143B spheroids to invade the matrix highlights their aggressive phenotype and validates the suitability of this 3D model for studying tumor-stroma interactions and invasion dynamics. In contrast, MG63 cells retained their compact spheroid morphology throughout the observation period, highlighting their lower invasiveness [17]. These engineered hydrogel beads offer a reproducible and scalable platform for modelling tumor microenvironments and assessing cell behavior in biologically relevant 3D settings.

3.2. *Effect of Lic-A on hydrogel bead metabolism and viability*

Lic-A, known for its antitumoral activity, was tested on the established 3D model. Due to the fast proliferation rate of 143B, treatments were performed at day 5 for 143B (80 μM) or day 7 for MG63 cells (120 μM). Concentrations were selected based on previously published data in 3D cultures [13]. As shown in Fig. 2**E**, an increase in the PI red fluorescence indicates a loss of membrane integrity in the spheroids of both tumor cell lines. Interestingly, WS1 human dermal fibroblasts, labelled in green, appeared largely unaffected by the treatment. This observation is in line with previous finding [18]. Metabolic activity, presented in Fig. 2**F**, showed a significant reduction after 48 h of treatment, corroborating the viability data.

The enhanced effect in the 3D model, compared to previously published data [13], may be partially explained by the smaller spheroid size, likely improving Lic-A penetration and uniform distribution throughout the spheroids. Smaller spheroids typically lack hypoxic or necrotic cores that often contribute to therapeutic resistance, and their higher surface-area-to-volume ratio increases drug exposure [19]. In addition, the highly invasive behavior of the 143B cell line led to progressive disintegration of the spheroid structure, with tumor cells spreading throughout the surrounding matrix. As a result, the classical spheroid morphology was lost, and cells were more dispersed within the hydrogel. This loss of compact architecture further enhanced drug sensitivity by reducing cell-cell interactions and by exposing a larger number of tumor cells directly to Lic-A [19].

To further validate our co-culture system and to investigate the effects of Lic-A on healthy bone tissue, we improved the model by incorporating BM-MSCs instead of dermal fibroblasts. This modification allowed us to more accurately mimic the bone microenvironment and to assess the potential cytotoxicity of Lic-A toward non-tumoral bone-related cells. In these experiments, we focused on the 143B OS cell line. As shown in Figs. 3**A** and 3**B**, BM-MSCs exhibited good proliferation overtime, confirming the suitability of these cells for the model. Following the treatment with Lic-A, a clear dose-dependent response was observed **(**Fig. 3**C-D)**. Fluorescence imaging revealed an increase in red staining, indicative of cell death, particularly in the OS cells. Importantly, at lower concentrations, Lic-A demonstrated higher toxicity toward 143B tumor cells compared to the healthy BM-MSC counterpart, suggesting a degree of selective cytotoxicity. Although these findings are preliminary and require further mechanistic investigation, they provide an important indication that Lic-A may preferentially target OS cells while exerting limited toxicity on normal bone-related cells.

3.3. *143B hydrogel bead model characterization*

Since 143B cells exhibit a pronounced invasive capacity and given that metastasis remains one of the major challenges in current OS therapy [20], we have focused further investigation of 143B model. To monitor cells spreading from the spheroid, live-cell imaging was performed (Fig. 4**A**, Video 1**S)**. For this experiment, 143B cells were stained green, and images were acquired every 4 h between 48 and 84 h post-encapsulation. The time-lapse imaging revealed that a significant spreading occurred within 36 h (Fig. 4**B**). The area occupied by the spheroids increased threefold in 60 h, from approximately 60,000 to 180,000 μm^2. The rapid matrix infiltration observed likely reflects their aggressive metastatic phenotype, potentially driven by enhanced expression of matrix metalloproteinases (MMPs), cytoskeletal remodeling, and interactions with the ECM.

To further characterize the system, hydrogel stiffness was evaluated at different time points (Fig. 4**C**). At day 1, acellular hydrogels displayed a mean stiffness of 5.9 ± 1.1 kPa, compared with 4.33 ± 1.25 kPa in cell-seeded hydrogels. In both groups, stiffness decreased significantly over time, consistent with a progressive softening of the matrix under culture conditions. At day 5, stiffness values dropped to 3.7 ± 1.1 kPa in acellular hydrogels and 1.1 ± 0.7 kPa in cell-seeded hydrogels, with the difference between groups reaching statistical significance. This observation suggests that the presence of cells may promote matrix remodeling and/or degradation, thereby accelerating stiffness reduction. By day 7, stiffness further declined to 1.7 ± 0.4 kPa and 1.3 ± 0.6 kPa in acellular and cell-seeded hydrogels, respectively, confirming the time-dependent loss of mechanical integrity. Collectively, these results indicate that both culture time and cell presence modulate hydrogel mechanical properties, which may in turn influence the biological

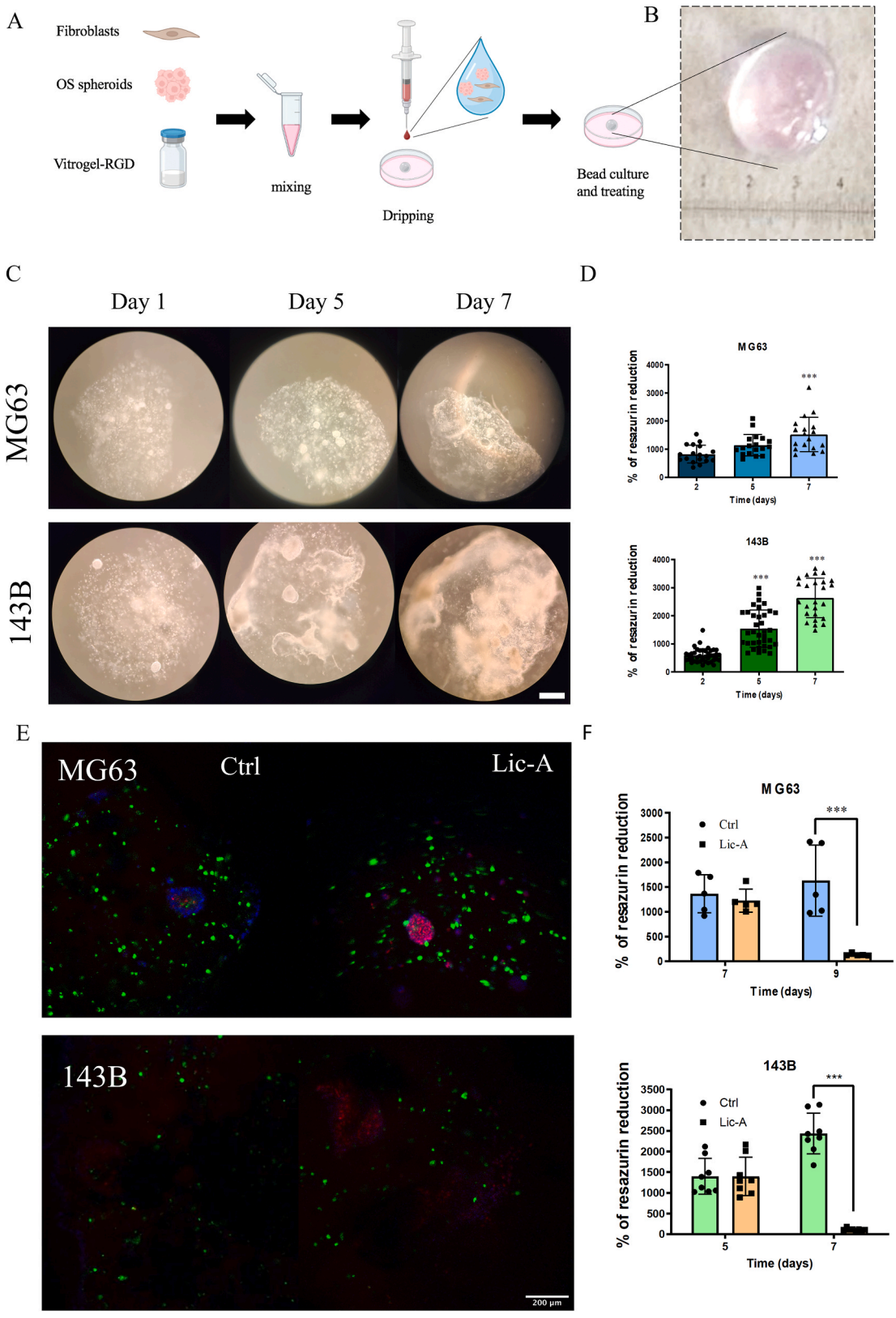

Fig. 2. Effect of Lic-A on hydrogel bead viability. A) Schematic representation of hydrogel bead preparation. B) Sample picture of an hydrogel bead. C) Representative microscopic images at 1, 5 and 7 days. Scale bar 500 µm. D) Metabolic activity of MG63 and 143B hydrogel beads at 2, 5 and 7 days. Data are reported as mean ± SD (MG63 n = 18, 143B n = 25). One-way ANOVA test against day 2 was conducted. E). Representative confocal image acquired after 48 h treatment with Lic-A of hydrogel beads. WS1 cells were stained with DiO (green), nuclei with Hoechst (blue), and dead cells with PI (red). Scale bar 200 µm. F) Metabolic activity of hydrogel beads after 48 h treatment with Lic-A. Values are expressed as mean ± SD (MG63 n = 5, 143B n = 8). Two-way ANOVA test against control was conducted.

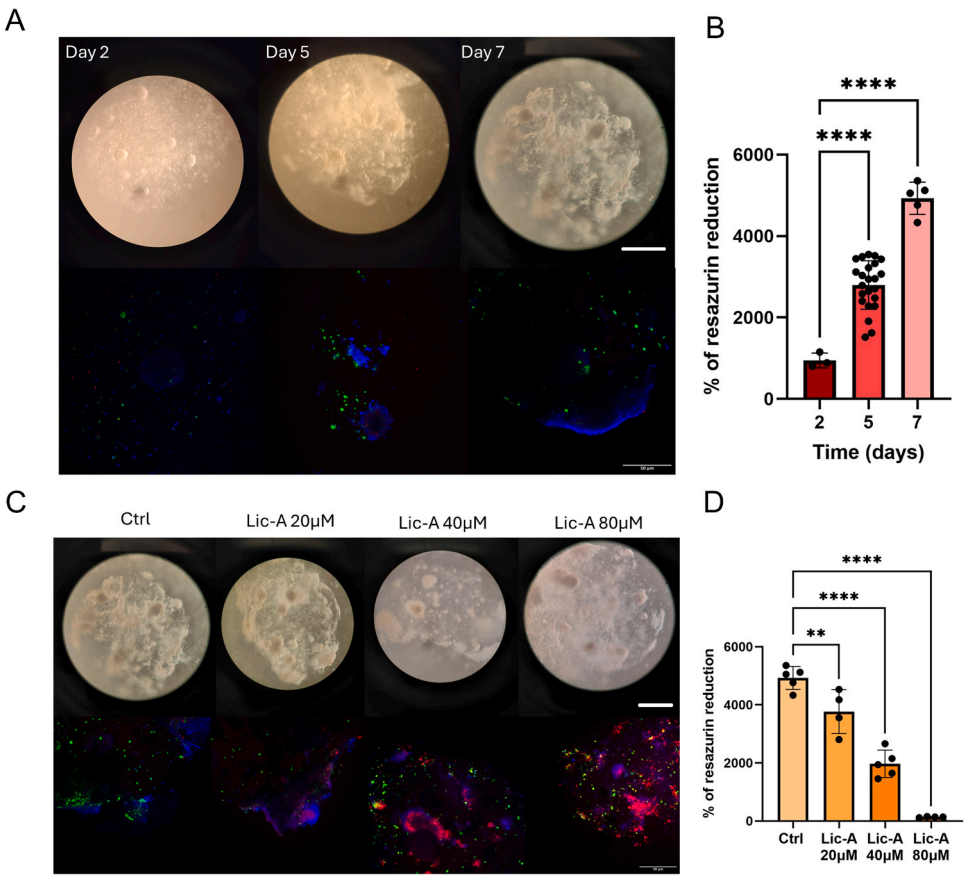

Fig. 3. Characterization of the 3D hydrogel beads model and response to Lic-A treatment. A) Representative micrographs and confocal images at 1, 5 and 7 days. BM-MSCs were stained with DiO (green), nuclei with Hoechst (blue). Micrographs scale bar 500 μm and confocal images scale bar 50 μm. B) Metabolic activity of 143B hydrogel beads at 2, 5 and 7 days. Data are reported as mean ± SD (n = 3). One-way ANOVA against day 2 was conducted. C) Representative micrographs and confocal image acquired after 48 h treatment with Lic-A of hydrogel beads. BM-MSCs were stained with DiO (green), nuclei with Hoechst (blue), and dead cells with PI (red). Micrographs scale bar 500 μm and confocal images scale bar 50 μm. D) Metabolic activity of hydrogel beads after 48 h treatment with Lic-A. Values are expressed as mean ± SD (n = 4). Two-way ANOVA against control was conducted.

performance of the system. Importantly, matrix stiffness is a key regulator of tumor cell behavior, influencing adhesion, migration, cytoskeletal organization, and extracellular matrix remodeling. In this context, the lower stiffness observed in cell-seeded hydrogels, particularly at day 5, supports the hypothesis that 143B cells actively remodel their surrounding microenvironment. Although the present analysis does not fully dissect the bidirectional relationship between matrix mechanics and invasive behavior, it demonstrates that the mechanical properties of the hydrogel are dynamic rather than static and should therefore be considered when interpreting tumor progression within this model.

Consistent with these mechanical changes, environmental scanning electron microscopy (ESEM) images, acquired at day 4 and 10 days, further confirmed the invasive nature of 143B cells in the 3D hydrogel system overtime (Fig. 4**D**). The high-resolution images revealed extensive cell-matrix interactions, with 143B cells exhibiting protrusive structures such as filopodia and lamellipodia extending into the surrounding matrix (asterisk in Fig. 3B). These features are hallmarks of active cancer cell migration and ECM remodeling, consistent with their aggressive phenotype observed in live-cell imaging. Microscopic analysis also suggests degradation patterns in the hydrogel network and localized matrix breakdown probably mediated by MMPs. These ultrastructural insights complement our live imaging data and provide additional evidence of dynamic cellular behavior within the matrix. Collectively, these findings validate the robustness of our 3D model in mimicking early metastatic processes and support its utility for probing tumor invasion at both cellular and morphological levels.

To assess cytoskeletal organization, F-actin staining was performed (Fig. 4**E-F**). In control samples, well-defined F-actin filaments were observed, with cells exhibiting intact intercellular connections. Conversely, samples treated with Lic-A displayed marked disruption and disorganization of F-actin structures. These results corroborate previous findings demonstrating Lic-A-induced cytoskeletal alterations in 2D culture systems [21]. Moreover, nuclear morphology in treated cells revealed pyknosis and apoptotic features, consistent with the induction of programmed cell death. The pro-apoptotic effects of Lic-A have been extensively reported in various cancer models [22], including OS [21, 23].

A related study described the development of 3D culture systems using bioprinting technologies, specifically employing the drop-on-demand technique to fabricate tissue constructs for clinical and drug development applications [24]. In that model, 143B cells were encapsulated in an alginate hydrogel, where they maintained high viability and formed tumor-like structures by day 7. In the present study, we introduced a more physiologically relevant 3D system based on the VitroGel® RGD matrix, which supports enhanced cell–matrix interactions. This environment promoted early and sustained invasive behavior of 143B OS cells co-cultured with stromal WS1 fibroblasts, with matrix infiltration observed as early as days 3–4 and complete by day 7 (see Figs. 2**C and** 3**A**).

Taken together, the live-cell imaging, mechanical characterization, and ESEM observations indicate that the model captures not only tumor cell invasion in a spatially relevant 3D setting, but also the associated dynamic remodeling of the surrounding microenvironment. This aspect

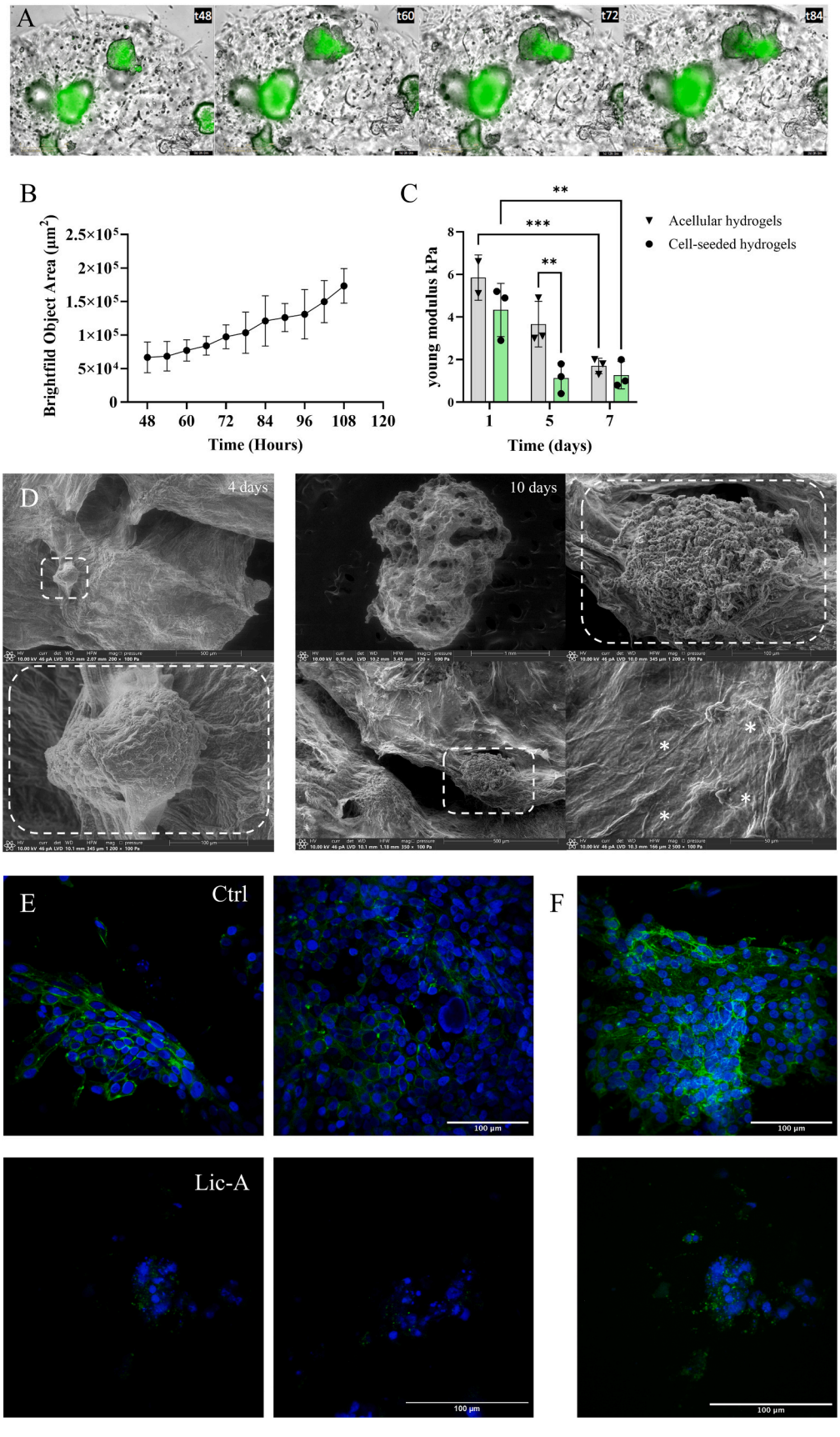

(caption on next page)

Fig. 4. 143B hydrogel beads characterization. A) Representative phase contrast images acquired at different times with IncuCyte® live imaging instrument. 143B cells were stained green with DiO. Scale bar 400 μm B) Measurement of spheroids and invasion at different time points through IncuCyte® Software. C) Dynamic mechanical analysis hydrogels characterization (Young's Moduli) at different time points. Data are reported as mean ± SD (n = 3). Two-way ANOVA was conducted. D) Representative SEM images of the beads acquired at different magnification after 4 and 7 days of culture; E) Representative confocal microscopy images and F) Z projection (maximum intensity). Nuclei were stained with Hoechst (blue) and f-actin filaments were stained with phalloidin (green). Scale bar 100 μm.

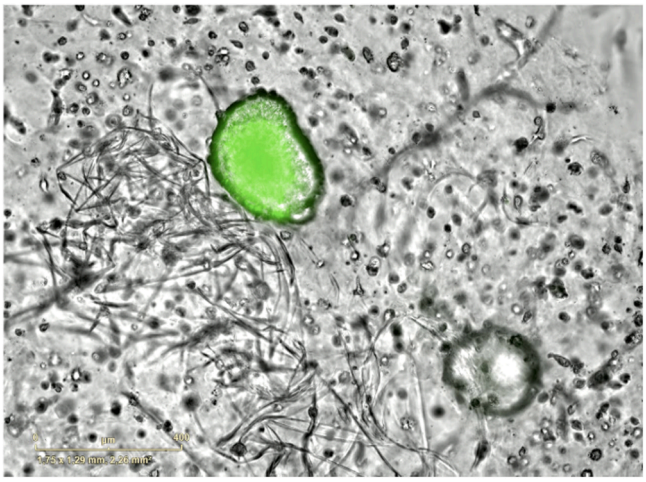

Video 1. A video clip is available online. Supplementary material related to this article can be found online at doi:10.1016/j.biopha.2026.119485.

is particularly relevant in OS, where invasive progression is strongly influenced by reciprocal tumor-matrix interactions. Therefore, the present platform provide a useful intermediate system between conventional 2D cultures and *in vivo* preclinical models for investigating both phenotypic responses and matrix-dependent mechanisms of invasion.

3.4. Lic-A reduce cells metabolism and viability in a concentration-dependent manner

To evaluate whether the effect of Lic-A was dose-dependent, two complementary assays were performed to assess cell viability and cytotoxicity (Fig. 5**)**. Notably, treatment with 40 μM Lic-A resulted in a significant reduction in metabolic activity, with an approximate decrease of 50% compared to controls. These findings were further supported by the LDH release assay, which detects lactate dehydrogenase enzyme released from damaged cells as a marker of membrane integrity loss [25]. Consistent with the viability data, LDH activity increased progressively with higher Lic-A concentrations, indicating that the reduction in metabolic activity was accompanied by dose-dependent cytotoxicity. Together, these assays confirm that Lic-A exerts a cytotoxic effect in a concentration-dependent manner, highlighting its potential as an anti-tumor agent.

3.5. Effect of Lic-A on expression of tumorigenic marker

To focus on the effect of Lic-A on the metastatic process, the expression of selected markers was analyzed by real-time PCR and immunofluorescence. Gene expression analysis was performed at 20 μM, and the results are presented in Fig. 6**A**. A significant reduction in Ki67 expression, a well-established marker of cell proliferation [26], was observed in treated samples ($p = 0.0053$), confirming the anti-proliferative effect of Lic-A. The expression of MMP-9, a matrix metalloproteinase associated with tumor invasion [27], was significantly downregulated in the treated group compared to the control ($p = 0.0003$), suggesting that Lic-A inhibits invasion by reducing MMP-9 expression. In contrast, MMP-2, another key protease involved in ECM degradation and metastatic spread, showed no significant change, suggesting that Lic-A exerts a selective inhibitory effect primarily on MMP-9 mediated invasive pathways [27]. Unexpectedly, the expression of vimentin, a classical marker of EMT [28], was significantly upregulated ($p = 0.0025$). The expression of BMP2, a key signaling molecule involved in bone formation and regeneration, plays a crucial role in osteogenic differentiation and skeletal development [29], was determined.

Interestingly, the expression of BMP-2, was significantly upregulated following treatment ($p < 0.0003$), which may reflect a compensatory or differentiation-related response to Lic-A exposure. The expression of COL1A1, a major component of the ECM in bone [30], was higher in control samples than in treated ones. Although the reduction in COL1A1 expression did not reach statistical significance, the trend supports a potential role for Lic-A in modulating matrix remodeling and limiting tumor invasion.

Gene expression analysis revealed a significant upregulation of VEGF-C in Lic-A treated samples compared to controls ($p < 0.0001$), while VEGF-A expression showed a slight, non-significant decrease. VEGF is a crucial factor in angiogenesis and vasculogenesis, primarily affecting endothelial cells. It plays a vital role in maintaining vascular homeostasis in various tissues and contributes significantly to the molecular pathogenesis of metastasis and tumor progression [31]. VEGF exerts its effects by binding to its receptor, VEGFR, which activates downstream signaling pathways that include the induction of MMPs. These enzymes degrade the ECM, thereby facilitating new blood vessel formation. Among the VEGF family members, VEGF-A plays a dominant role in angiogenesis and is implicated in several pathological conditions, while VEGF-C and VEGF-D are more specifically associated with lymphangiogenesis [32]. In this context, the differential regulation of

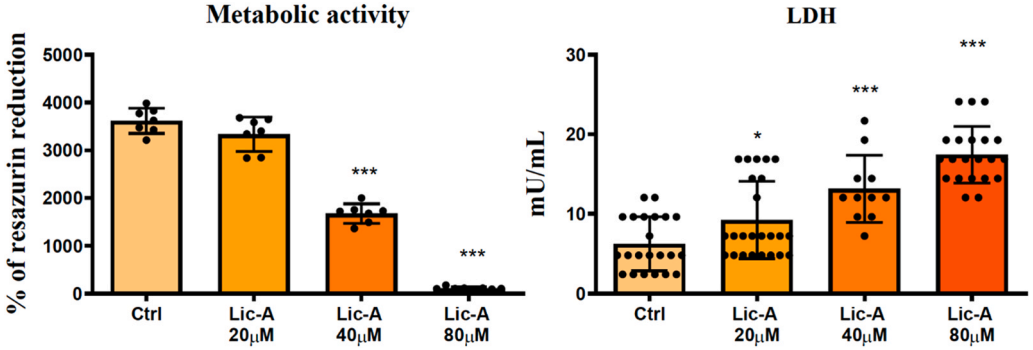

Fig. 5. Dose response determination. Metabolic activity (left) and LDH (right) assay after 48 h treatment with Lic-A at 20, 40 and 80 μM were analyzed. Values are expressed as mean ± SD (Metabolic activity n = 7, LDH assay n = 11). One-way ANOVA against control was conducted.

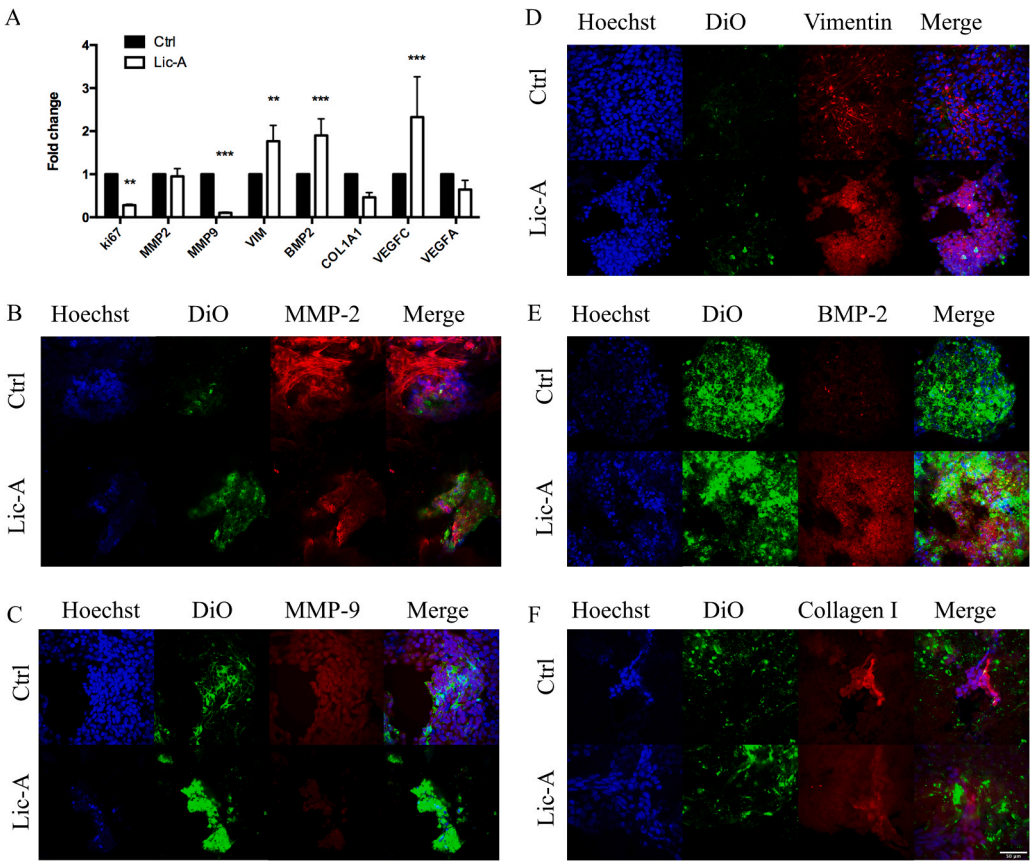

Fig. 6. Effects of Licochalcone A on proliferation and invasion markers in 143B cells. A) RT-PCR analysis of Ki67, MMP2, MMP9, VIM, BMP2, COL1A1, VEGFC and VEGFA after 48 h treatment with 20 μM of Lic-A. Data are presented as mean ± SD (n = 4). Two-way ANOVA against control was conducted; B-F) Immunofluorescence staining after 48 h of treatment with 20 μM of Lic-A. Nuclei were stained in blue, 143B in green and different markers in red. Scale Bar 50 μm.

VEGF-C and VEGF-A observed here suggests that Lic-A may influence angiogenic and lymphangiogenic signaling in a complex manner, which deserves further investigation.

To further validate the effects of Lic-A at the protein level, immunofluorescence staining was performed. The expression patterns of MMP2, MMP9, BMP2 and COL1A1 were consistent with mRNA expression levels obtained by RT-PCR, confirming the downregulation of MMP9, the unchanged MMP2 and COL1A1 and the upregulation of BMP2 following treatment (Fig. 6**B, C, E and F**).

Interestingly, although vimentin mRNA levels increased following Lic-A treatment, immunofluorescence staining revealed a disorganized and fragmented filamentous structure (Fig. 6**D**). This effect may be due to post-transcriptional and/or post-translational modifications or apoptosis-related cytoskeletal degradation, both of which disrupt vimentin assembly. Alternatively, the upregulation of vimentin may reflect a stress-induced compensatory response rather than an active EMT program. These findings suggest that Lic-A interferes with cytoskeletal integrity not only at the transcriptional level but also at the structural level. This is consistent with previous studies showing that vimentin filaments are susceptible to caspase-mediated cleavage and disassembly during apoptosis, [33]. This can lead to fragmented or collapsed cytoskeletal structure, even when mRNA expression is upregulated. Additionally, stress-induced overexpression of vimentin has been reported as part of a non-productive or maladaptive EMT-like response, particularly in drug-treated or damaged cells [34,35]. Although the upstream signaling pathways modulated by Lic-A were not directly investigated in the present study, our findings are consistent with previous reports describing the pleiotropic anti-tumoral activity of this compound in several cancer models [22], including OS [21,23]. Indeed, Lic-A has been associated with the regulation of signaling pathways involved in cell proliferation, apoptosis, migration, and extracellular matrix remodeling, such as PI3K/Akt [36], MAPK [37], NF-kB [38], and STAT3-related cascades [39]. Within this framework, the reduction in Ki67 and MMP-9 expression observed in our 3D model, together with the disruption of cytoskeletal organization and the presence of apoptotic nuclear features, supports the hypothesis that Lic-A interferes with pathways controlling both tumor cell survival and invasive behavior. Nevertheless, dedicated mechanistic studies will be required to determine which of these signaling axes are specifically responsible for the effects observed in our 3D OS model. Overall, these findings highlight the potential of Lic-A as a therapeutic agent that effectively targets multiple aspects of OS progression, including proliferation, invasion, and EMT, thereby offering promising avenues for future anti-metastatic strategies. At the same time, these results further support the utility of our 3D model as a more physiologically relevant platform than 2D culture systems for investigating tumor behavior and drug response.

The presented model validates the inhibitory role of Lic-A in a more physiologically relevant setting compared to 2D monolayers. However, to enhance the clinical relevance of our findings, it is crucial to consider the inherent heterogeneity of the TME and its impact on antitumor immunity. The spatial organization within our hydrogel beads provides a more realistic representation of cell-cell interactions compared to 2D cultures, yet the absence of immune components remains a limitation for studying immune-evasion mechanisms [40]. Furthermore, given the metastatic propensity of 143B cells towards the lung and bone, our model could be further implemented to test targeted delivery strategies [41]. Specifically, addressing signaling axes such as CXCL12-CXCR4, a master regulator of OS metastasis, within a bioengineered TME could provide key insights into anti-metastatic therapeutic interventions [42].

In conclusion, while our 3D bioengineered platform currently focuses on the phenotypic characterization of OS cell behavior, its ability to recapitulate key aspects of the metastatic microenvironment opens significant avenues for more complex co-culture systems and personalized medicine. By addressing the limitations related to immune components and mechanical characterization, this model can evolve into a high-throughput tool for identifying novel therapeutic targets and validating delivery systems specifically designed for the bone niche.

4. Conclusion

Here, we established an *in vitro* OS model based on hydrogel beads that better mimics the TME, by incorporating tumor and stromal components. By selecting VitroGel® RGD as the encapsulating matrix, we enable effective cell–matrix interactions, particularly supporting fibroblast viability and tumor cell invasion. The production of uniform, small-size spheroids allowed their homogeneous distribution and integration into the hydrogel beads and allowed for precise, controlled drug treatment protocols.

The model allows effectively distinguished between OS cell lines of differing invasive potential, with 143B spheroids demonstrating spreading and matrix infiltration, in contrast to the more compact and less invasive morphology of MG63 spheroids. This phenotypic divergence underlines the model's capability to recapitulate tumor heterogeneity and invasion dynamics in a physiologically relevant context.

Treatment with Lic-A revealed marked anti-tumoral activity in the 3D system, including significant reductions in viability, metabolic activity, and cytoskeletal integrity. Notably, the pronounced therapeutic effect compared to prior 3D models may be due to the smaller spheroid size and increased drug accessibility, as well as disruption of protective cell-cell interactions during invasion. Together, these factors highlight the importance of considering spheroid size, structure, and invasion dynamics when investigating drug efficacy in 3D models.

Molecular analysis further confirmed that Lic-A downregulated key pro-metastatic markers, such as MMP-9 and Ki67, while altering the expression of EMT-related proteins, including disorganized vimentin filaments and increased BMP-2.

Overall, our findings demonstrate that this OS model is a relevant platform to investigate OS biology (invasion, tumor-stroma interactions, and drug responsiveness) and provides a promising alternative to traditional 2D cultures as a tool for preclinical screening of anti-metastatic compounds.

CRediT authorship contribution statement

Rossi M.: Conceptualization, Data curation, Formal Analysis, Methodology, Visualization, Writing-original draft. **Anconelli L.:** Investigation, Methodology. **Rydzyk M.M.:** Investigation, Methodology. **Crea A.:** Investigation, Data curation. **Rossi F.:** Data curation, Visualization. **Coschina E.:** Investigation, Methodology. **Ravegnini G.:** Data curation, Validation, Writing- review and editing. **Ulian G.:** Investigation, Methodology. **Valdrè G.:** Methodology. **Montesi M.:** Methodology, Validation. **Gardini D.:** Formal analysis, Methodology. **Cappadone C.:** Supervision, Validation, Writing- review and editing. **Blasi P.:** Validation, Writing- review and editing, Funding acquisition. **Iotti S.:** Supervision, Project administration, Writing- review and editing. **Malucelli E.** Funding acquisition, Supervision, Writing- review and editing.

Funding

This research was supported by the Italian Ministry of Health (Ministero della Salute) within the framework of the project *"Sviluppo di approcci innovativi ed alternativi alla modellistica animale in ambito tossicologico, oncologico e per disturbi del neurosviluppo"*. Specifically, the activities were conducted under Work Package 5 (WP5): *"Modelli complessi tridimensionali di osteosarcoma umano per sostituire la sperimentazione animale negli studi preclinici"* (Principal Investigator: Prof. Emil Malucelli).

Additional funding was provided by PRIN – Progetti di Ricerca di Rilevante Interesse Nazionale, Bando 2022, Prot. 2022WKNWRF, financed by the Italian Ministry of University and Research (MUR) and Bando Ricerca Scientifica e Alta Tecnologia 2024, Cod. SIME: 2024.0350, financed by Fondazione CARISBO (P.I. Prof. Emil Malucelli). Moreover, Emma Coschina acknowledges support from the European Union - NextGenerationEU, through the Italian Ministry of University and Research (PNRR-M4C2-I1.3), Project PE_00000019 *"HEAL ITALIA"*, CUP J33C22002920006.

Declaration of Competing Interest

The authors declare that they have no known competing financial interests or personal relationships that could have appeared to influence the work reported in this paper.

Acknowledgements

We thank Center for Applied Biomedical Research (CRBA), University of Bologna for technical and scientifical support.

Appendix A. Supporting information

Supplementary data associated with this article can be found in the online version at doi:10.1016/j.biopha.2026.119485.

Data availability

Data will be made available on request.

References

1 M. Zhra, S.A. Akhund, K.S. Mohammad, Advancements in osteosarcoma therapy: overcoming chemotherapy resistance and exploring novel pharmacological strategies, Pharmers 18 (2025), https://doi.org/10.3390/ph18040520.
2 G. Ottaviani, N. Jaffe, The epidemiology of osteosarcoma, Cancer Treat. Res 152 (2009) 3–13, https://doi.org/10.1007/978-1-4419-0284-9_1.
3 J. Hoarau-Vechot, A. Rafii, C. Touboul, J. Pasquier, Halfway between 2D and animal models: are 3D cultures the ideal tool to study cancer-microenvironment interactions? Int J. Mol. Sci. 19 (2018) https://doi.org/10.3390/ijms19010181.
4 M. Rossi, P. Blasi, Multicellular tumor spheroids in nanomedicine research: a perspective, Front. Med. Technol. 4 (2022) 909943, https://doi.org/10.3389/fmedt.2022.909943.
5 J. Cui, D. Dean, F.J. Hornicek, Z. Chen, Z. Duan, The role of extracelluar matrix in osteosarcoma progression and metastasis, J. Exp. Clin. Cancer Res. 39 (2020) 178, https://doi.org/10.1186/s13046-020-01685-w.
6 J. Rodrigues, B. Sarmento, C.L. Pereira, Osteosarcoma tumor microenvironment: the key for the successful development of biologically relevant 3D in vitro models, Vitr. Models (2022), https://doi.org/10.1007/s44164-022-00008-x, 5-27, 10.1007/s44164-022-00008-x.
7 A. De Luca, L. Raimondi, F. Salamanna, V. Carina, V. Costa, D. Bellavia, R. Alessandro, M. Fini, G. Giavaresi, Relevance of 3d culture systems to study osteosarcoma environment, J. Exp. Clin. Cancer Res. 37 (2018) 2, https://doi.org/10.1186/s13046-017-0663-5.
8 L. Tan, Y. Wang, X. Hu, G. Du, X. Tang, L. Min, Advances of osteosarcoma models for drug discovery and precision medicine, Biomolecules 13 (2023), https://doi.org/10.3390/biom13091362.
9 M.V. Monteiro, V.M. Gaspar, L.P. Ferreira, J.F. Mano, Hydrogel 3D in vitro tumor models for screening cell aggregation mediated drug response, Biomater. Sci. 8 (2020) 1855–1864, https://doi.org/10.1039/c9bm02075f.
10 M. Rimann, S. Laternser, A. Gvozdenovic, R. Muff, B. Fuchs, J.M. Kelm, U. Graf-Hausner, An in vitro osteosarcoma 3D microtissue model for drug development, J. Biotechnol. 189 (2014) 129–135, https://doi.org/10.1016/j.jbiotec.2014.09.005.
11 S. Costa, J. Rodrigues, C. Vieira, S. Dias, J. Viegas, F. Castro, B. Sarmento, C. L. Pereira, Advancing osteosarcoma 3D modeling for novel tumor microenvironment-targeted therapies development, J. Control. Release 376 (2024) 1068–1085, https://doi.org/10.1016/j.jconrel.2024.10.068.
12 M.T. Li, L. Xie, H.M. Jiang, Q. Huang, R.S. Tong, X. Li, X. Xie, H.M. Liu, Role of licochalcone a in potential pharmacological therapy: a review, Front. Pharm. 13 (2022) 878776, https://doi.org/10.3389/fphar.2022.878776.
13 M. Rossi, C. Pellegrino, M.M. Rydzyk, G. Farruggia, D. de Biase, S. Cetrullo, S. D'Adamo, A. Bisi, P. Blasi, E. Malucelli, et al., Chalcones induce apoptosis,

autophagy and reduce spreading in osteosarcoma 3D models, Biomed. Pharm. 179 (2024) 117284, https://doi.org/10.1016/j.biopha.2024.117284.
14 Valdrè, G.; Moro, D.; Ulian, G. Monte Carlo simulation of the effect of shape and thickness on SEM-EDS microanalysis of asbestos fibres and bundles: the case of anthophyllite, tremolite and actinolite. In Proceedings of IOP Conf. Ser.: Mater. Sci. Eng.; p. 012019.
15 D. Moro, G. Ulian, V. G, Monte Carlo SEM-EDS micro- and nanoanalysis of ultrathin gold leaves in glass mosaic tesserae: thickness effects and measurement strategy, Measurement 129 (2018) 211–217.
16 H. Kurihara, T. Nagamune, Cell adhesion ability of artificial extracellular matrix proteins containing a long repetitive Arg-Gly-Asp sequence, J. Biosci. Bioeng. 100 (2005) 82–87, https://doi.org/10.1263/jbb.100.82.
17 A.B. Mohseny, I. Machado, Y. Cai, K.L. Schaefer, M. Serra, P.C. Hogendoorn, A. Llombart-Bosch, A.M. Cleton-Jansen, Functional characterization of osteosarcoma cell lines provides representative models to study the human disease, Lab Invest 91 (2011) 1195–1205, https://doi.org/10.1038/labinvest.2011.72.
18 M. Rossi, C. Cappadone, G. Picone, A. Bisi, G. Farruggia, F. Belluti, P. Blasi, S. Gobbi, E. Malucelli, Natural-like Chalcones with Antitumor Activity on Human MG63 Osteosarcoma Cells, Molecules 27 (2022), https://doi.org/10.3390/molecules27123751.
19 S.J. Han, S. Kwon, K.S. Kim, Challenges of applying multicellular tumor spheroids in preclinical phase, Cancer Cell Int. 21 (2021) 152, https://doi.org/10.1186/s12935-021-01853-8.
20 G. Sheng, Y. Gao, Y. Yang, H. Wu, Osteosarcoma and Metastasis, Front Oncol. 11 (2021) 780264, https://doi.org/10.3389/fonc.2021.780264.
21 T.S. Shen, Y.K. Hsu, Y.F. Huang, H.Y. Chen, C.P. Hsieh, C.L. Chen, Licochalcone A suppresses the proliferation of osteosarcoma cells through autophagy and ATM-Chk2 activation, Molecules 24 (2019), https://doi.org/10.3390/molecules24132435.
22 J. Wang, Y.S. Zhang, K. Thakur, S.S. Hussain, J.G. Zhang, G.R. Xiao, Z.J. Wei, Licochalcone A from licorice root, an inhibitor of human hepatoma cell growth via induction of cell apoptosis and cell cycle arrest, Food Chem. Toxicol. 120 (2018) 407–417, https://doi.org/10.1016/j.fct.2018.07.044.
23 R.C. Lin, S.F. Yang, H.L. Chiou, S.C. Hsieh, S.H. Wen, K.H. Lu, Y.H. Hsieh, Licochalcone A-induced apoptosis through the activation of p38MAPK pathway mediated mitochondrial pathways of apoptosis in human osteosarcoma cells in vitro and in vivo, Cells 8 (2019), https://doi.org/10.3390/cells8111441.
24 B.E. Grottkau, Z. Hui, Y. Pang, A novel 3D bioprinter using direct-volumetric drop-on-demand technology for fabricating micro-tissues and drug-delivery, Int. J. Mol. Sci. 21 (2020), https://doi.org/10.3390/ijms21103482.
25 C. Korzeniewski, D.M. Callewaert, An enzyme-release assay for natural cytotoxicity, J. Immunol. Methods 64 (1983) 313–320, https://doi.org/10.1016/0022-1759(83)90438-6.
26 X. Sun, P.D. Kaufman, Ki-67: more than a proliferation marker, Chromosoma 127 (2018) 175–186, https://doi.org/10.1007/s00412-018-0659-8.
27 K. Bjornland, K. Flatmark, S. Pettersen, A.O. Aaasen, O. Fodstad, G.M. Maelandsmo, Matrix metalloproteinases participate in osteosarcoma invasion, J. Surg. Res 127 (2005) 151–156, https://doi.org/10.1016/j.jss.2004.12.016.
28 K. Strouhalova, M. Prechova, A. Gandalovicova, J. Brabek, M. Gregor, D. Rosel, Vimentin intermediate filaments as potential target for cancer treatment, Cancers (Basel) 12 (2020) 184, https://doi.org/10.3390/cancers12010184.
29 A. Nguyen, M.A. Scott, S.M. Dry, A.W. James, Roles of bone morphogenetic protein signaling in osteosarcoma, Int Orthop. 38 (2014) 2313–2322, https://doi.org/10.1007/s00264-014-2512-x.
30 B. Brodsky, A.V. Persikov, Molecular structure of the collagen triple helix, Adv. Protein Chem. 70 (2005) 301–339, https://doi.org/10.1016/S0065-3233(05)70009-7.
31 T. Assi, S. Watson, B. Samra, E. Rassy, A. Le Cesne, A. Italiano, O. Mir, Targeting the VEGF Pathway in Osteosarcoma, Cells 10 (2021) 1240, https://doi.org/10.3390/cells10051240.
32 R.S. Apte, D.S. Chen, N. Ferrara, VEGF in Signaling and Disease: Beyond Discovery and Development, Cell 176 (2019) 1248–1264, https://doi.org/10.1016/j.cell.2019.01.021.
33 J.E. Eriksson, T. He, A.V. Trejo-Skalli, A.S. Harmala-Brasken, J. Hellman, Y.H. Chou, R.D. Goldman, Specific in vivo phosphorylation sites determine the assembly dynamics of vimentin intermediate filaments, J. Cell Sci. 117 (2004) 919–932, https://doi.org/10.1242/jcs.00906.
34 N. Mor-Vaknin, A. Punturieri, K. Sitwala, D.M. Markovitz, Vimentin is secreted by activated macrophages, Nat. Cell Biol. 5 (2003) 59–63, https://doi.org/10.1038/ncb898.
35 M.I. Kokkinos, R. Wafai, M.K. Wong, D.F. Newgreen, E.W. Thompson, M. Waltham, Vimentin and epithelial-mesenchymal transition in human breast cancer–observations in vitro and in vivo, Cells Tissues Organs 185 (2007) 191–203, https://doi.org/10.1159/000101320.
36 J.P. Tsai, C.H. Lee, T.H. Ying, C.L. Lin, C.L. Lin, J.T. Hsueh, Y.H. Hsieh, Licochalcone A induces autophagy through PI3K/Akt/mTOR inactivation and autophagy suppression enhances Licochalcone A-induced apoptosis of human cervical cancer cells, Oncotarget 6 (30) (2015) 28851–28866, https://doi.org/10.18632/oncotarget.4767.
37 X. Fan, G. Guan, J. Wang, M. Jin, L. Wang, X. Duan, Licochalcone A induces cell cycle arrest and apoptosis via suppressing MAPK signaling pathway and the expression of FBXO5 in lung squamous cell cancer, Oncol. Rep. 50 (6) (2023) 214, https://doi.org/10.3892/or.2023.8651.
38 J.P. Tsai, P.C. Hsiao, S.F. Yang, S.C. Hsieh, D.T. Bau, C.L. Ling, C.L. Pai, Y.H. Hsieh, Licochalcone A suppresses migration and invasion of human hepatocellular carcinoma cells through downregulation of MKK4/JNK via NF-κB mediated urokinase plasminogen activator expression, PLoS One 9 (1) (2014) e86537, https://doi.org/10.1371/journal.pone.0086537.
39 J. Seo, D.E. Lee, S.M. Kim, E. Kim, J.K. Kim, Licochalcone A Exerts Anti-Cancer Activity by Inhibiting STAT3 in SKOV3 Human Ovarian Cancer Cells, Biomedicines 11 (5) (2023) 1264, https://doi.org/10.3390/biomedicines11051264.
40 Y. Fang, Y. Kong, G. Rong, Q. Luo, W. Liao, D. Zeng, Systematic Investigation of Tumor Microenvironment and Antitumor Immunity With IOBR, Med Res. 1 (2025) 136–140, https://doi.org/10.1002/mdr2.70001.
41 M. Long, X. Liu, X. Huang, M. Lu, X. Wu, L. Weng, Q. Chen, X. Wang, L. Zhu, Z. Chen, Alendronate-functionalized hypoxia-responsive polymeric micelles for targeted therapy of bone metastatic prostate cancer, J. Control Release 334 (2021) 303–317, https://doi.org/10.1016/j.jconrel.2021.04.035.
42 P. Yang, Y. Hu, Q. Zhou, The CXCL12-CXCR4 signaling axis plays a key role in cancer metastasis and is a potential target for developing novel therapeutics against metastatic cancer, Curr. Med. Chem. 27 (33) (2020) 5543–5561, https://doi.org/10.2174/0929867326666191113113110.